



Article

A Cd(II) Luminescent Coordination Grid as a Multiresponsive Fluorescence Sensor for Cr(VI) Oxyanions and Cr(III), Fe(III), and Al(III) in Aqueous Medium

 Kuo-Shun Liao ¹, Meng-Jung Tsai ¹, Li-Jen Hsu ¹, Chih-Min Wang ^{2,3,*}  and Jing-Yun Wu ^{1,*} 

¹ Department of Applied Chemistry, National Chi Nan University, Nantou 545, Taiwan; aasd6307@gmail.com (K.-S.L.); s97324905@mail1.ncnu.edu.tw (M.-J.T.); Doadadam1996@gmail.com (L.-J.H.)
² Department of Bioscience and Biotechnology, National Taiwan Ocean University, Keelung 202, Taiwan
³ General Education Center, National Taiwan Ocean University, Keelung 202, Taiwan
 * Correspondence: cmwang@ntou.edu.tw or twcmwang@gmail.com (C.-M.W.); jyunwu@ncnu.edu.tw (J.-Y.W.)

Abstract: Hydro(solvo)thermal reactions of Cd(NO₃)₂, *N*-(pyridin-3-ylmethyl)-4-(pyridin-4-yl)-1,8-naphthalimide (NI-mbpy-34), and 5-bromobenzene-1,3-dicarboxylic acid (Br-1,3-H₂bdc) afforded a luminescent coordination polymer, [Cd(Br-1,3-bdc)(NI-mbpy-34)(H₂O)]·2H₂O]_{*n*} (**1**). Single-crystal X-ray diffraction analysis showed that **1** features a two-dimensional (2-D) gridlike *sql* layer with the point symbol of (4⁴·6²), where the Cd(II) center adopts a [CdO₅N₂] pentagonal bipyramidal geometry. Thermogravimetric (TG) analysis confirmed the thermal stability of **1** up to about 340 °C, whereas XRPD patterns proved the maintenance of crystallinity and framework integrity of **1** in CH₂Cl₂, H₂O, CH₃OH, and toluene. Photoluminescence studies indicated that **1** displayed intense blue fluorescence emissions in both solid-state and H₂O suspension-phase. Owing to the good fluorescent properties, **1** could serve as an excellent turn-off fluorescence sensor for selective and sensitive Cr(VI) detection in water, with LOD = 15.15 μM for CrO₄²⁻ and 14.91 μM for Cr₂O₇²⁻, through energy competition absorption mechanism. In addition, **1** could also sensitively detect Cr³⁺, Fe³⁺, and Al³⁺ ions in aqueous medium via fluorescence-enhancement responses, with LOD = 2.81 μM for Cr³⁺, 3.82 μM for Fe³⁺, and 3.37 μM for Al³⁺, mainly through an absorbance-caused enhancement (ACE) mechanism.

Keywords: coordination polymer; Cr(VI) oxyanion; luminescence sensor; trivalent metal ion



Citation: Liao, K.-S.; Tsai, M.-J.; Hsu, L.-J.; Wang, C.-M.; Wu, J.-Y. A Cd(II) Luminescent Coordination Grid as a Multiresponsive Fluorescence Sensor for Cr(VI) Oxyanions and Cr(III), Fe(III), and Al(III) in Aqueous Medium. *Molecules* **2021**, *26*, 7103. <https://doi.org/10.3390/molecules26237103>

Academic Editors: Emilio Pardo, Jesús Ferrando Soria and Edwin Charles Constable

Received: 14 October 2021

Accepted: 22 November 2021

Published: 24 November 2021

Publisher's Note: MDPI stays neutral with regard to jurisdictional claims in published maps and institutional affiliations.



Copyright: © 2021 by the authors. Licensee MDPI, Basel, Switzerland. This article is an open access article distributed under the terms and conditions of the Creative Commons Attribution (CC BY) license (<https://creativecommons.org/licenses/by/4.0/>).

1. Introduction

With the advanced development of modern society, rapid industrial and agricultural productions and rich human activities have increasingly brought about severe chemical pollution. Among various chemical pollutants, heavy metal ion based inorganic contaminants are of higher concern compared with other contaminants such as organic pollutants due to their nondegradability and bioaccumulation [1]. Moreover, heavy metal ions are well-known poisonous contaminants in water due to their high toxicity, which could cause serious environmental and ecological harm and cause a detrimental effect on human health [2]. For example, chromium exists in aquatic environments usually in the forms of Cr(VI) oxyanions, i.e., dichromate (Cr₂O₇²⁻) and chromate (CrO₄²⁻) ions, and/or free cation, i.e., trivalent Cr(III) ion. The Cr(VI) oxyanions are highly carcinogenic and mutagenic, causing hereditary genetic defects and various types of cancers [3–5]. While the Cr(III) ion is essentially harmless due to its low toxicity, it may, however, cause mutations and malignant cells when excessive accumulation occurs [5–7]. The permissible limit for Cr(VI) in drinking water is set as 50 μg/L by the World Health Organization (WHO) [8]. Iron and aluminum are two ubiquitous metals widely used in daily applications around human living environments [9]. Trivalent Fe(III) and Al(III) cations are the forms of iron and aluminum that can enter human body. As one of the most important elements for living

organisms, Fe(III) ion influences a variety of vital bioprocesses such as electron transfer, oxygen storage, oxygen metabolism, among others [10–12]. The deficiency or excess of Fe(III) ion is harmful to human health, resulting in some diseases [13–15]. Additionally, Al(III) ion in body fluids is toxic to humans and will induce harmful effects that cause diseases such as Alzheimer's disease and Parkinson's disease when its content in the body is over an acceptable standard [9,12,16]. The tolerable daily ingestion of Al^{3+} for the human body is about 3–10 mg/day [7] and the permissible level in drinking water is set as 7.41 μM by the WHO [17].

In recent years, the sensing and detection of chemical pollutants has attracted tremendous interest from many researchers. Benefitting from their unique merits, low-cost, easy manipulation, instant, visual identification, excellent sensitivity, and high selectivity [7,12], fluorescence based detection has gained considerable attention among various conventional instrumental techniques. Nowadays, various advanced fluorescence sensory materials have emerged, such as organic dyes [18], quantum dots (QDs) [19,20], and carbon dots (CDs) [21,22], among others. Of particular note is one kind of organic–inorganic hybrid material called coordination polymers (CPs), fabricated by metal ions or clusters as nodes and bridging organic ligands as linkers through the connection of coordination bonds. As a matter of fact, luminescent CP-based chemo/biosensors have been actively used to detect small molecules, explosives, ions, gas, and pH, among others, and several reviews have been devoted to the sensory properties [23–29]. Recently, we have made advances in fluorescence detection of hazardous chemical contaminants by using luminescent organic–inorganic hybrid materials as sensory platforms [30–39]. Herein, we report a new Cd(II) based luminescent CP, $\{[\text{Cd}(\text{Br}-1,3\text{-bdc})(\text{NI}\text{-mbpy}\text{-}34)(\text{H}_2\text{O})]\cdot 2\text{H}_2\text{O}\}_n$ (**1**), where NI-mbpy-34 = *N*-(pyridin-3-ylmethyl)-4-(pyridin-4-yl)-1,8-naphthalimide, Br-1,3-H₂bdc = 5-bromobenzene-1,3-dicarboxylic acid. The solid-state structure of **1** has a simple two-dimensional (2-D) layer structure adopting a gridlike net with the point symbol of $(4^4\cdot 6^2)$, which is highly stable in water. The remarkable emission properties make **1** a functional multiresponsive fluorescence sensor for Cr(VI) oxyanions detection via a quenching effect, and Cr(III), Fe(III), and Al(III) sensing via an enhancement response in aqueous medium, with high sensitivity and remarkable selectivity.

2. Experimental Section

2.1. Materials and Characterization

All of the chemicals and solvents were acquired from market sources (MATRIX, ULTRA, ACROS, PanReac Applichem, SHOWA, Fluka, VETEC, ALFA, MACRON, J.T. Baker, SIGMA ALDRICH), and used without further processing. Ligand NI-mbpy-34 was synthesized according to the previously reported literature [40]. Thermogravimetric (TG) analyses were performed using a Thermo Cahn VersaTherm HS TG analyzer (Thermo, Newington, NH, USA) under flow nitrogen with a heating rate of 5 °C/min. X-ray powder diffraction (XRPD) patterns were measured using a Shimadzu XRD-7000 diffractometer (Shimadzu, Kyoto, Japan) with a graphite monochromatized Cu K α radiation ($\lambda = 1.5406 \text{ \AA}$) at 30 kV and 30 mA. Infrared (IR) spectroscopic measurements were performed on a Perkin-Elmer Frontier Fourier transform infrared spectrometer (Perkin-Elmer, Taipei, Taiwan) using attenuated total reflection (ATR) technique. Fluorescence spectroscopic measurements were performed at room temperature using a Hitachi F7000 fluorescence spectrophotometer (Hitachi, Tokyo, Japan) equipped with a 150 W xenon lamp as an excitation source. UV-Vis absorption spectra were recorded at room temperature using a JASCO V-750 UV/VIS spectrophotometer (JASCO, Tokyo, Japan). Elemental microanalyses (C, H, N) were performed on an Elementar Vario EL III analytical instrument (Elementar, Langensfeld, Germany). Ultrasonic agitation of suspensions was conducted using a Qsonica Q125 instrument. X-ray photoelectron spectroscopy (XPS) analyses were performed on an ULVAC-PHI PHI 5000 VersaProbe/Scanning ESCA Microprobe instrument (ULVACPHI Inc., Kanagawa, Japan).

2.2. Synthesis of $\{[Cd(Br-1,3-bdc)(NI-mbpy-34)(H_2O)] \cdot 2H_2O\}_n$ (**1**)

A DMF solution (2 mL) of NI-mbpy-34 (9.1 mg, 0.025 mmol), an aqueous solution (2 mL) of $Cd(NO_3)_2 \cdot 4H_2O$ (15.4 mg, 0.050 mmol), and a DMF solution of Br-1,3-H₂bdc (12.3 mg, 0.050 mmol) were sequentially added into an acid digestion bomb placed in a Teflon-lined stainless steel autoclave. The mixture was kept inside a furnace at 80 °C for 48 h and then cooled to ambient temperature. Yellowish crystals suitable for X-ray diffraction were collected after washing with distilled water and ethanol, and dried at room temperature. Yield: 60% based on NI-mbpy-34 (12.1 mg, 0.015 mmol). IR (ATR, cm^{-1}): 3072, 1590, 1460, 1333, 992, 889, 723. Anal. Calcd. for $C_{31}H_{24}BrCdN_3O_9$: C, 48.01; H, 3.09; N, 5.42%. Found: C, 48.24; H, 2.94; N, 5.41%. The phase purity of the bulky sample was confirmed by the closely matched XRPD patterns between the simulated pattern, calculated from single-crystal diffraction data and the experimental pattern of as-synthesized **1** without grinding (Figure S1). Of particular note, the XRPD patterns of the same microcrystalline sample after grinding showed alternations in intensity, and in some peak positions, compared to the simulated XRPD patterns. This is tentatively attributed to the influences of either the variation in preferred orientation of the powdered sample [30] or the partial crystal structure distortion caused by grinding [41] or both.

2.3. Single-Crystal X-ray Structure Determinations

The diffraction data were collected using a Bruker D8 Venture diffractometer configured with a PHOTO100 CMOS detector at 150(2) K, equipped with a graphite monochromated Mo K α radiation ($\lambda = 0.71073 \text{ \AA}$). The structures were solved by direct methods with the SHELXTL program [42] and refined by full-matrix least-squares methods on F^2 using the SHELXL-2014/7 [43], incorporated in WINGX [44] crystallographic collective package. Non-hydrogen atoms were refined with anisotropic displacement parameters, except where noted. Carbon-bound hydrogen atoms were calculated in ideal positions and refined as riding mode. Oxygen-bound hydrogen atoms were structurally evident in the difference Fourier map. All of the hydrogen atoms were refined with isotropic displacement parameters, U_{iso} , constrained to be 1.2 or 1.5 times U_{eq} of the carrier atom. Experimental details for X-ray data collection and the refinements are summarized in Table 1. Hydrogen-bonding parameters are shown in Table S1. CCDC 1991627 (**1**) contain the supplementary crystallographic data for this paper. These data can be obtained free of charge from the Cambridge Crystallographic Data Centre via www.ccdc.cam.ac.uk/data_request/cif (accessed on 19 March 2020).

Table 1. X-ray data collection and structure refinement for **1**.

Empirical Formula	$C_{31}H_{24}BrCdN_3O_9$
M_w	774.84
Crystal system	Triclinic
Space group	$P\bar{1}$
$a, \text{ \AA}$	10.169(3)
$b, \text{ \AA}$	11.285(4)
$c, \text{ \AA}$	14.502(4)
$\alpha, ^\circ$	97.526(10)
$\beta, ^\circ$	107.465(10)
$\gamma, ^\circ$	108.503(10)
$V, \text{ \AA}^3$	1457.8(8)
Z	2
$T, \text{ K}$	150(2)
$\lambda, \text{ \AA}$	0.71073
$D_{calc}, \text{ g cm}^{-3}$	1.765
F_{000}	772
$\mu, \text{ mm}^{-1}$	2.182
Reflns collected	44,573
Unique reflns (R_{int})	5934(0.0424)

Table 1. Cont.

Empirical Formula	C ₃₁ H ₂₄ BrCdN ₃ O ₉
Obsd reflns ($I > 2\sigma(I)$)	5201
Params	406
R_1^a ($I > 2\sigma(I)$)	0.0289
wR_2^b ($I > 2\sigma(I)$)	0.0601
R_1^a (all data)	0.0368
wR_2^b (all data)	0.0646
GOF on F^2	1.152
$\Delta\rho_{\max}, \Delta\rho_{\min}, e \text{ \AA}^{-3}$	1.015, -0.561

$$^a R_1 = \sum ||F_o| - |F_c|| / \sum |F_o|; ^b wR_2 = \{ \sum [w(F_o^2 - F_c^2)] / \sum [w(F_o^2)] \}^{1/2}.$$

3. Results and Discussion

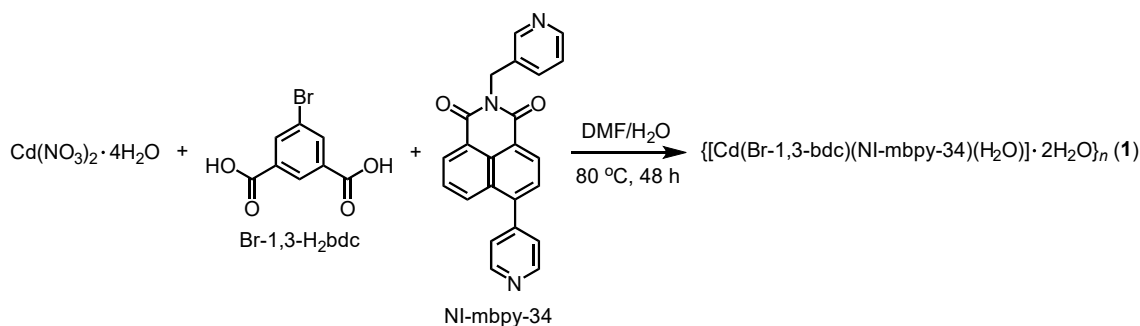
3.1. Synthesis and Crystal Structure of $\{[Cd(Br-1,3-bdc)(NI-mbpy-34)(H_2O)] \cdot 2H_2O\}_n$ (1)

Hydro(solvo) thermal reactions of $Cd(NO_3)_2 \cdot 4H_2O$, Br-1,3-H₂bdc, and NI-mbpy-34 in DMF/H₂O media afforded **1** as yellowish crystals (Scheme 1). Single-crystal X-ray structure analysis reveals that the crystal structure of **1** belongs to the triclinic space group $P\bar{1}$. The asymmetric unit contains one Cd(II) center, one Br-1,3-bdc²⁻ dianion, one NI-mbpy-34 ligand, and one coordination and two lattice water molecules (Figure 1a). The Cd(II) center adopts a $\{CdO_5N_2\}$ pentagonal bipyramidal geometry, where the equatorial plane is made up of two carboxylate groups of two distinct Br-1,3-bdc²⁻ dianions in one asymmetric (Cd1–O3 = 2.254(2) Å, Cd1–O4 = 2.753 Å) and one symmetric (Cd1–O5#2 = 2.393(2) Å, Cd1–O6#2 = 2.389(2) Å, #2, $x - 1, y, z$) chelating modes and one 4-pyridyl nitrogen atom (naphthalene end) from one NI-mbpy-34 ligand (Cd1–N3 = 2.301(2) Å), while the two apical positions are located by one coordination water molecule (Cd1–O7 = 2.348(2) Å) and one 3-pyridyl nitrogen atom (imide end) from the other NI-mbpy-34 ligand (Cd1–N2#1 = 2.354(3) Å, #1, $x + 1, y + 1, z + 1$). Each Br-1,3-bdc²⁻ dianion adopts a μ_2 -Br-1,3-bdc- $\kappa O, O' : \kappa O, O'$ mode to bridge two Cd(II) centers, where the two carboxylate groups suit an asymmetric and a symmetric chelating coordination mode (Figure 1a). Connection of Cd(II) centers by Br-1,3-bdc²⁻ dianions and NI-mbpy-34 ligands simultaneously forms a two-dimensional (2-D) gridlike layer (Figure 1b), which can be simplified as a 4-connected **sql** net with the point symbol of $(4^4 \cdot 6^2)$ (Figure 1c). Two such gridlike layers with the coordination water molecules oriented face-to-face are linked together in pair through O–H...O hydrogen bonding interactions (O...O, 2.723(3) and 2.932(3) Å, Table S1) formed between the coordinated water molecules and the carboxylate oxygen atoms of the Br-1,3-bdc²⁻ ligands (Figure 1d), generating a 2-D hydrogen-bonded bilayer (Figure 1e). When viewed down the crystallographic [100] direction, there are small pores with potential sufficient solvent accessible voids of only about 9.8% of the unit cell volume [45], accompanied by lattice water molecules (Figure 1e). These lattice water molecules form hydrogen-bonding interactions with each other (O...O, 3.035(5) Å) and, importantly, with the framework (O...O, 2.839(5) and 2.855(4) Å) to expand the 2-D hydrogen-bonded bilayers to be the three-dimensional (3-D) hydrogen-bonded network (Figure 1e,f).

3.2. Chemical Stability and Thermal Properties

The chemical stability of **1** in different solvents including dichloromethane (CH₂Cl₂), *N,N'*-dimethylacetamide (DMAc), *N,N'*-dimethylformamide (DMF), H₂O, methanol (CH₃OH), and toluene was checked. After separately immersing **1** in CH₂Cl₂, H₂O, CH₃OH, and toluene for 24 h, the checked XRPD patterns of so-obtained powdered samples were very similar to the patterns of as-synthesized **1** after grinding, with slight differences in peak intensity (Figure 2). This might suggest the preferred orientation effect or the minor extent of partial distortion of the long range order in **1**. However, the checked XRPD patterns still imply the maintenance of framework integrity and crystallinity, con-

firming the high stability of **1**. In contrast, **1** displayed low stability after immersing in DMAc and DMF due to the poorly matched XRPD profiles.



Scheme 1. Synthesis of **1**.

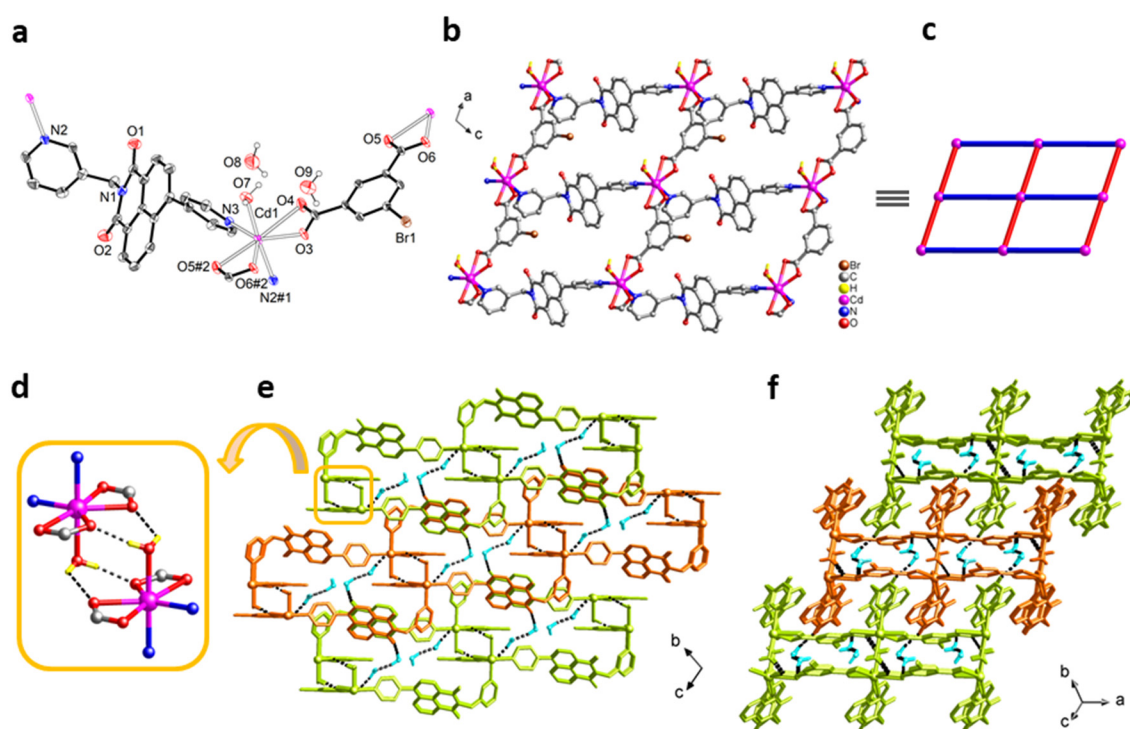


Figure 1. Crystal structure of **1**: (a) ORTEP plot of the asymmetry unit with thermal ellipsoids in 50% probability level, showing the coordination environment around the Cd(II) center and the coordination modes of the Br-1,3-bdc²⁻ and NI-mbpy-34 ligands. Symmetry codes: #1, $x + 1, y + 1, z + 1$; #2, $x - 1, y, z$; (b) a single 2-D gridlike layer; (c) schematic representation of the 4-connected **sql** grid; (d) highlight of the hydrogen bonding interactions between the coordinated water molecules and the carboxylate oxygen atoms of the Br-1,3-bdc²⁻ ligands; (e) representation of the 2-D hydrogen-bonded bilayers viewed down the crystallographic [100] direction, showing small pores accompanied by lattice water molecules; (f) representation of the lattice water molecules supported 3-D hydrogen-bonded network viewed down the [111] direction, showing the intercalated 2-D hydrogen-bonded bilayers.

Thermogravimetric (TG) analysis was performed under a nitrogen atmosphere to examine the thermal stability of **1** (Figure S2). The TG trace of **1** exhibited a weight loss of 5.4% from room temperature to 69 °C, corresponding to the escape of lattice water molecules (calcd. 4.6%). A gradual weight loss of 1.6% corresponding to the removal of coordinated water molecules (calcd. 2.3%) followed when the temperature was raised to approaching 186 °C. Then, the TG trace showed the existence of a stable plateau before the framework began to process a two-step collapse from ca. 340 °C to ca. 633 °C. Dur-

ing the decomposition, bromide might react with divalent cadmium to generate CdBr_2 (b.p. = 844 °C), which would escape at higher temperature. The final residue of 8.4% was reasonably assigned to the CdO component (calcd. 8.3%).

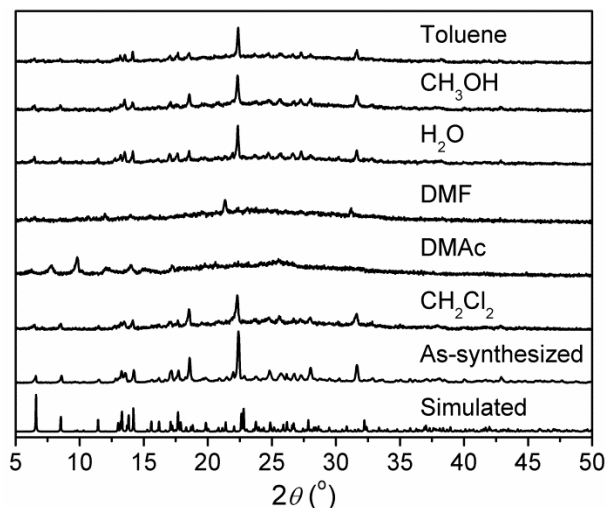


Figure 2. XRPD patterns of **1** before and after dispersing in different solvents for 24 h.

3.3. Gas Adsorption Properties of Activated **1**

In the crystal structure of **1**, there are free void spaces of about 9.8% of the unit cell volume, hence, the porous properties of activated **1** were investigated by gas adsorption studies. Prior to gas adsorption experiments, as-synthesized **1** (about 100 mg) was thermally treated at 100 °C under a reduced pressure for 24 h to remove solvent molecules and thus to give activated **1**. For activated **1**, N_2 adsorption isotherms exhibited no appreciable uptakes of $5.92 \text{ cm}^3 \text{ g}^{-1}$ STP at $P/P_0 = 1$ and 77 K, whereas CO_2 adsorption isotherms showed negligible uptakes of $11.19 \text{ cm}^3 \text{ g}^{-1}$ STP at $P/P_0 = 1$ and 195 K (Figure S3). The low N_2 and CO_2 uptakes of thermally activated **1** might be attributed to the small sufficient solvent-accessible voids and framework distortion induced pore-reduction, which resulted in surface adsorption. The latter assumption was supported by the checked XRPD patterns, which showed obvious differences with the experimental profiles of as-synthesized sample of **1** (Figure S4).

3.4. Photoluminescence Properties

When excited at $\lambda_{\text{ex}} = 370 \text{ nm}$, the solid-state emission spectrum of NI-mbpy-34 showed an intense emission band centered at 462 nm, which was overlapped with two further bands as shoulders at around 433 and 480 nm (Figure S5). After irradiation at $\lambda_{\text{ex}} = 360 \text{ nm}$, Br-1,3- H_2bdc emitted an extremely weak solid-state emission centered at around 468 nm. Comparably, **1** emitted intense blue fluorescence with an emission band centered at 436 nm in solid-state and 422 nm in H_2O suspension-phase upon excitation at $\lambda_{\text{ex}} = 365 \text{ nm}$. From the band position and shape, the emissions were tentatively assigned to the intraligand charge transfer of the NI-mbpy-34 ligand perturbed by metal coordination; this is further supported by the high resemblance in excitation spectra between NI-mbpy-34 and **1**.

3.5. Detection of Anions

In view of the high water stability and excellent fluorescence properties of **1** in H_2O suspension-phase, its potential ability to detect anions was explored in water. Anion detection studies were carried out by separately adding aqueous solutions of NaF and K_mX ($\text{X}^{m-} = \text{Cl}^-$, Br^- , I^- , ClO_4^- , CO_3^{2-} , $\text{Cr}_2\text{O}_7^{2-}$, CrO_4^{2-} , NO_3^- , and PO_4^{3-} , $m = 1, 2, 3$) into the well-prepared H_2O suspensions of **1**, with a concentration of 1 mM. Upon excitation at $\lambda_{\text{ex}} = 365 \text{ nm}$, the fluorescence detection results showed that most anions had

an inconspicuous fluorescence intensity change effect (<10% change) on **1**, except for the CO_3^{2-} , $\text{Cr}_2\text{O}_7^{2-}$, CrO_4^{2-} , and PO_4^{3-} ions (Figure 3). It is noted that CO_3^{2-} and PO_4^{3-} caused significant fluorescence enhancement by 63% and 44%, respectively. However, the two Cr(VI) oxyanions, $\text{Cr}_2\text{O}_7^{2-}$ and CrO_4^{2-} , showed obviously high quenching effects with an efficiency up to 97% and 99%, respectively, (quenching efficiency (%) = $(I_0 - I)/I_0 \times 100\%$, where I_0 and I are the maximum fluorescence intensities of **1** before and after addition of a quencher). Therefore, it is suggested to use the fluorescence quenching of **1** to detect trace amounts of $\text{Cr}_2\text{O}_7^{2-}$ and CrO_4^{2-} ions in water media. The anti-interference ability of **1** toward $\text{Cr}_2\text{O}_7^{2-}$ and CrO_4^{2-} was examined with the existence of different competitive anions in equal concentration. The competition experiments clearly indicated that $\text{Cr}_2\text{O}_7^{2-}$ and CrO_4^{2-} both retained high quenching ability to almost completely turn off the fluorescence of **1** when the other interference anions are present (Figure 4), implying high selectivity of **1** toward $\text{Cr}_2\text{O}_7^{2-}$ and CrO_4^{2-} over others perturbed anions in water media.

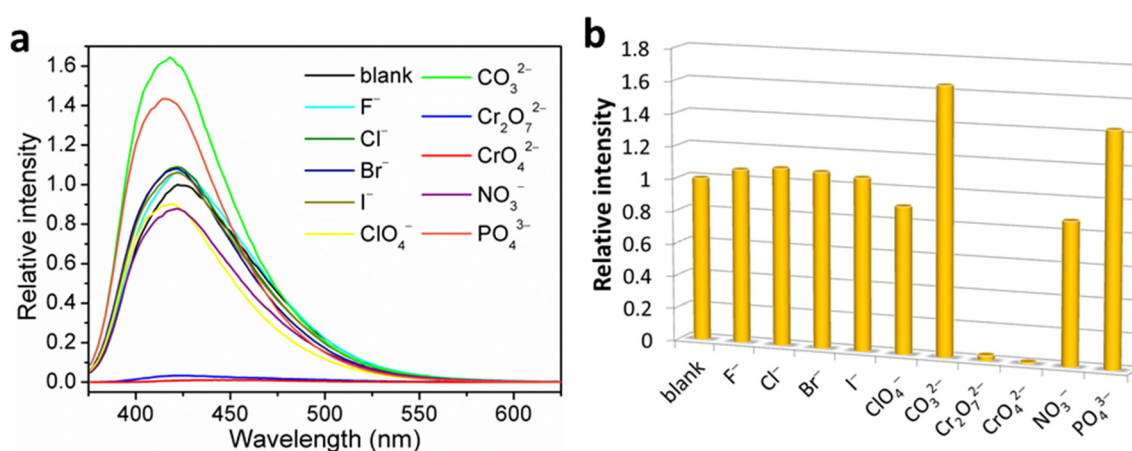


Figure 3. (a) Fluorescence spectra and (b) bar diagrams of **1** in H_2O suspension-phase upon addition of different anions at 1.0 mM when excited at $\lambda_{\text{ex}} = 365$ nm.

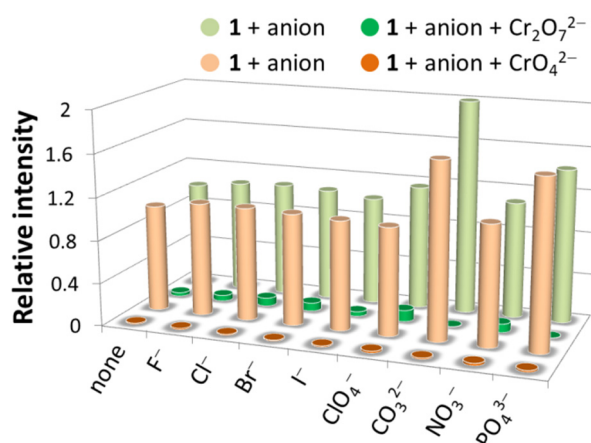


Figure 4. Bar diagrams to show luminescence quenching of **1** in H_2O suspension-phase for $\text{Cr}_2\text{O}_7^{2-}$ and CrO_4^{2-} ions with different perturbed anions in equal concentration (1.0 mM).

The sensitivity of Cr(VI) oxyanions detection in water media can be evaluated by quantitative analysis and limit of detection (LOD) values. The concentration-dependent fluorescence intensity of **1** was determined by gradually adding different concentrations of Cr(VI) oxyanion into well-dispersed H_2O suspensions of **1**. As observations, the fluorescence intensity of **1** gradually decreased with increasing concentration of $\text{Cr}_2\text{O}_7^{2-}$ and CrO_4^{2-} (Figure 5a,b), indicating that the fluorescence quenching of **1** caused by the

introduction of $\text{Cr}_2\text{O}_7^{2-}$ and CrO_4^{2-} ions can be quantified. It is also noted that the fluorescence intensity ($\lambda_{\text{em}} = 414 \text{ nm}$) versus the concentration of $\text{Cr}_2\text{O}_7^{2-}$ and CrO_4^{2-} can be well fitted to the first-order exponential decay (Figure S6), suggesting a diffusion-controlled fluorescence quenching. The fluorescence quenching efficiencies were further analyzed by a Stern–Volmer analysis based on the equation: $I_0/I = 1 + K_{\text{SV}}[\text{Q}]$, where I_0 and I are the fluorescence intensities before and after the addition of analytes, respectively, $[\text{Q}]$ is the molar concentration of the analyte (mM), and K_{SV} is the Stern–Volmer quenching constant (M^{-1}). The Stern–Volmer plots exhibited good linear correlations at low concentrations (inset in Figure 5c,d), which gave the K_{SV} values of $5.56 \times 10^3 \text{ M}^{-1}$ for $\text{Cr}_2\text{O}_7^{2-}$ and $1.32 \times 10^4 \text{ M}^{-1}$ for CrO_4^{2-} . Furthermore, the Stern–Volmer plots displayed upward deviation from linearity at high concentrations (Figure 5c,d), as a result of the combination of a dynamic energy transfer mechanism and a static self-absorption mechanism [46,47]. The LOD values for $\text{Cr}_2\text{O}_7^{2-}$ and CrO_4^{2-} were determined using the equation: $\text{LOD} = 3\sigma/k$, where σ is the standard deviation of five blank measurements of fluorescence for the H_2O suspensions of **1** and k is the absolute value of the slope of the calibration curve at low concentrations. The LOD values for $\text{Cr}_2\text{O}_7^{2-}$ and CrO_4^{2-} were determined to be 14.91 (3.22) and 15.15 (1.76) μM (ppm), respectively, (Figure S7). Owing to the excellent anti-interference ability and high K_{SV} and lower LOD values, **1** can be an effective fluorescence sensor displaying high detection selectivity and sensitivity toward $\text{Cr}_2\text{O}_7^{2-}$ and CrO_4^{2-} in water media.

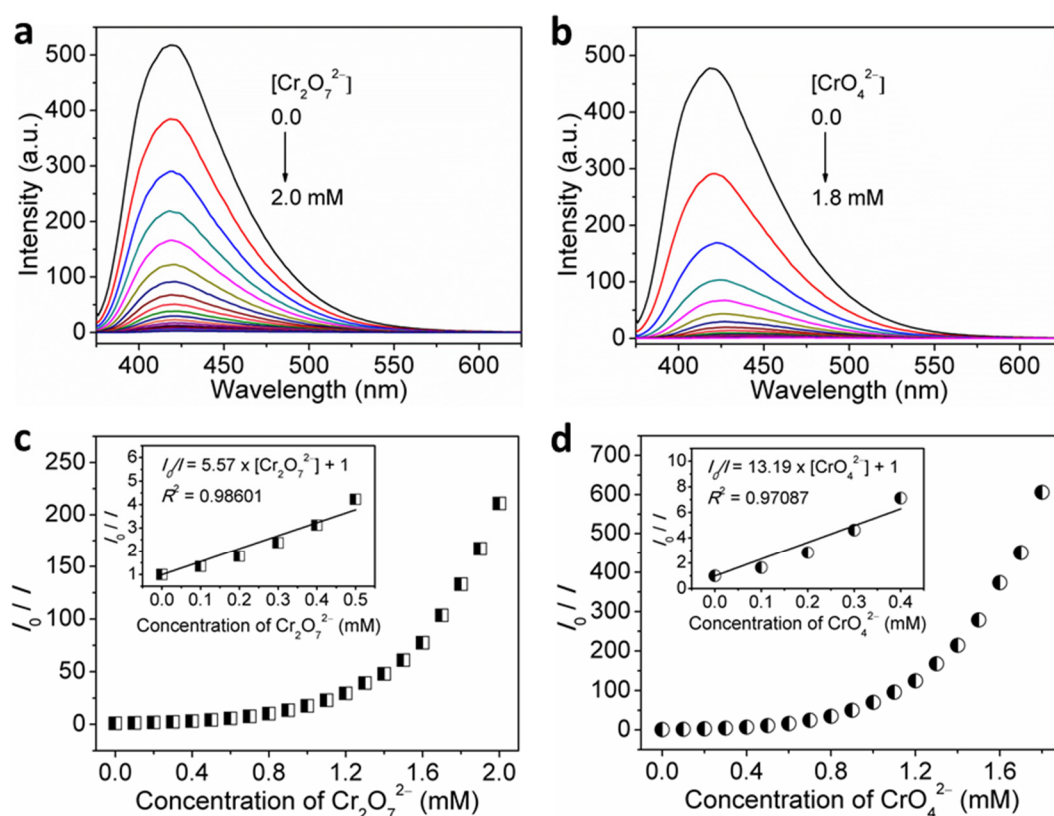


Figure 5. (a,b) Concentration-dependent fluorescence emission spectra of **1** in H_2O suspension-phase by incremental addition of $\text{Cr}_2\text{O}_7^{2-}$ and CrO_4^{2-} upon excitation at $\lambda_{\text{ex}} = 365 \text{ nm}$. (c,d) Stern–Volmer plot over the titration concentrations of $\text{Cr}_2\text{O}_7^{2-}$ and CrO_4^{2-} for **1** in H_2O suspension-phase. Inset: the linear Stern–Volmer plot at low $\text{Cr}_2\text{O}_7^{2-}$ and CrO_4^{2-} ion concentrations, where the solid line represents the linear fit to the Stern–Volmer equation.

3.6. Detection of Metal Ions

The influence of different metal ions on the fluorescent properties of **1** in H_2O suspension-phase was also investigated through similar procedures by adding well-prepared aqueous solutions of metal ions, including $\text{M}(\text{NO}_3)_n$ ($\text{M}^{n+} = \text{Ag}^+, \text{Al}^{3+}, \text{Mg}^{2+}$,

Ca^{2+} , Co^{2+} , Cr^{3+} , Cu^{2+} , Fe^{3+} , Na^+ , K^+ , Mn^{2+} , Ni^{2+} , and Pb^{2+} , $n = 1, 2, 3$), into the H_2O suspension of **1**, with a concentration of 1 mM. Upon excitation at $\lambda_{\text{ex}} = 365$ nm, interestingly, trivalent metal ions of Cr^{3+} , Fe^{3+} , and Al^{3+} have striking enhancement responses of 10.9, 5.4, and 5.4 times on the fluorescence intensity of **1** in H_2O suspension-phase, while other mono- and divalent metal ions have no or only minor effects (intensity change $\leq 10\%$) on the fluorescence intensity (Figure 6). It is also noteworthy that the addition of metal ions did not cause significant wavelength shift. To examine the selectivity of **1** toward Cr^{3+} , Fe^{3+} , and Al^{3+} , the interference experiments were carried out. After adding Cr^{3+} , Fe^{3+} , and Al^{3+} ions into the H_2O suspension of **1** containing other competitive metal ions in equal concentration, the fluorescence intensity of **1** in H_2O suspension-phase increased immediately but showed a certain degree of reduction in some cases, with a maximum of about 43% reduction compared to that without the co-existence of competitive metal ions (Figure 7). The observations indicated that changes in intensity for sensing Cr^{3+} , Fe^{3+} , and Al^{3+} were somewhat negatively affected, but still within acceptable limits, by the competitive metal ions. As a result, **1** displayed accessible anti-interference ability and detection selectivity for recognizing Cr^{3+} , Fe^{3+} , and Al^{3+} over other competitive metal ions.

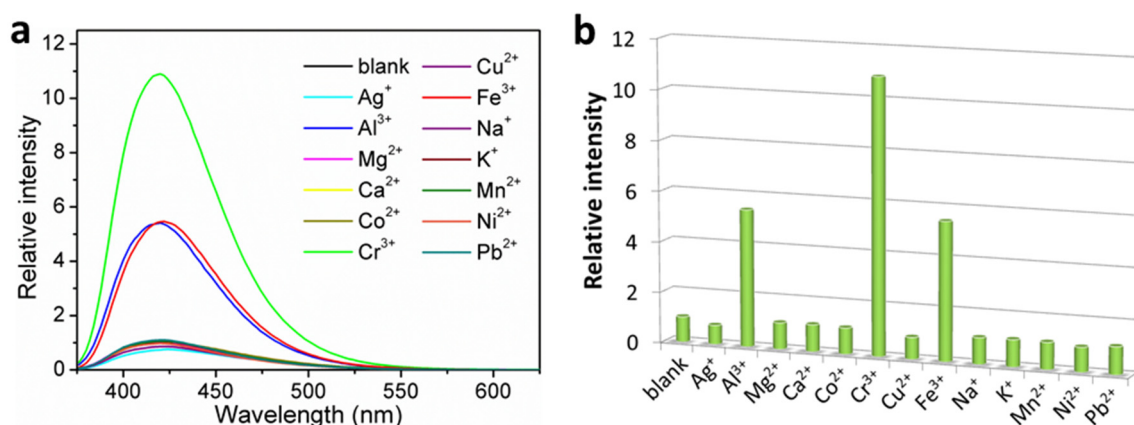


Figure 6. (a) Fluorescence spectra and (b) bar diagrams of **1** in H_2O suspension-phase upon addition of different metal ions at 1.0 mM when excited at $\lambda_{\text{ex}} = 365$ nm.

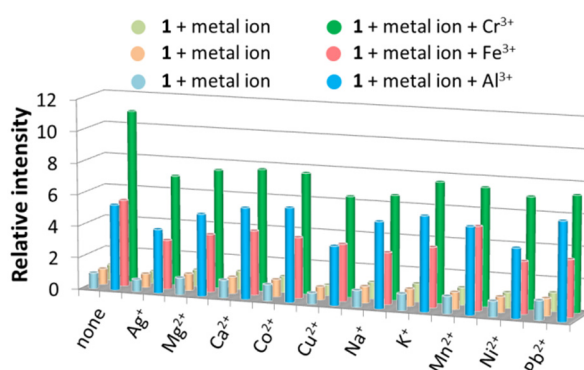


Figure 7. Bar diagrams to show fluorescence enhancement of **1** in H_2O suspension-phase for Cr^{3+} , Fe^{3+} , and Al^{3+} ions with different competitive metal ions in equal concentration (1.0 mM).

To further quantitatively evaluate the fluorescence response of **1** in H_2O suspension-phase toward Cr^{3+} , Fe^{3+} , and Al^{3+} , fluorescence titration for the above three metal ions was also investigated. It was observed that the fluorescence intensity of **1** in H_2O suspension-phase increased gradually upon incremental addition of the aqueous solutions of Cr^{3+} , Fe^{3+} , and Al^{3+} ions (Figure 8a–c). The fluorescence intensity ($\lambda_{\text{em}} = 414$ nm) obeyed the first-order exponential decay relationship with the concentration of Cr^{3+} , Fe^{3+} , and Al^{3+} (Figure 8d–f), suggesting diffusion-controlled fluorescence enhancement. The curvi-

linear dependence between I and concentration of metal ion conforms to the equation $I = -2611.22 \times \exp(-[\text{Cr}^{3+}]/0.31) + 2845.97$ ($R^2 = 0.9956$) for Cr^{3+} detection, $I = -2671.16 \times \exp(-[\text{Fe}^{3+}]/0.90) + 2895.00$ ($R^2 = 0.9909$) for Fe^{3+} detection, and $I = -2414.09 \times \exp(-[\text{Al}^{3+}]/0.85) + 2590.77$ ($R^2 = 0.9972$) for Al^{3+} detection. Moreover, there is a linear relationship between the fluorescence intensity of **1** in H_2O suspension-phase and the Cr^{3+} concentration in the range of 0–0.4 mM, the Fe^{3+} concentration in the range of 0–0.6 mM, and the Al^{3+} concentration in the range of 0–0.7 mM (Figure S8), suggesting that **1** could potentially quantitatively determine Cr^{3+} , Fe^{3+} , and Al^{3+} ions. Accordingly, the LOD is calculated to be 2.81 (146.2) μM (ppb) for Cr^{3+} detection, 3.82 (198.7) μM (ppb) for Fe^{3+} detection, and 3.37 (90.9) μM (ppb) for Al^{3+} detection, through the equation of $3\sigma/k$.

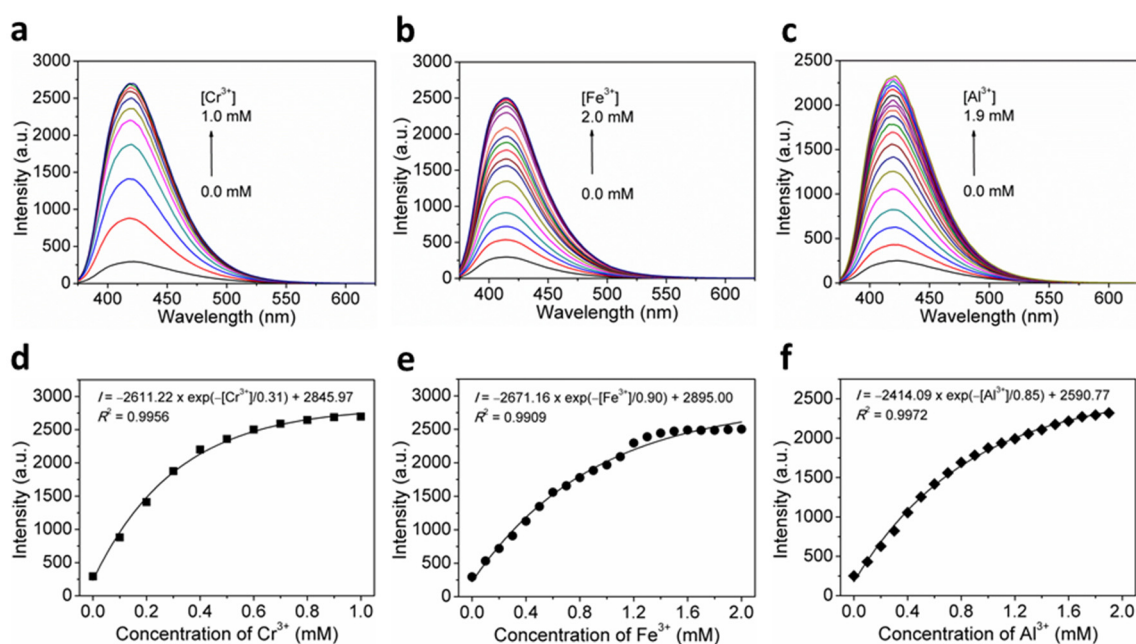


Figure 8. (a–c) Concentration-dependent fluorescence emission spectra of **1** in H_2O suspension-phase by incremental addition of Cr^{3+} , Fe^{3+} , and Al^{3+} ions upon excitation at $\lambda_{\text{ex}} = 365$ nm. (d–f) Plot of fluorescence intensity at $\lambda_{\text{em}} = 414$ nm versus Cr^{3+} , Fe^{3+} , or Al^{3+} ion concentration for **1** in H_2O suspension-phase, showing the first-order exponential decay.

3.7. Fluorescence-Responsive Sensing Mechanisms

Herein, the possible fluorescence-responsive sensing mechanisms are elucidated. For Cr(VI) oxyanions detection, the XRPD patterns of **1** treated with $\text{Cr}_2\text{O}_7^{2-}$ and CrO_4^{2-} in water were closely matched to that of as-synthesized **1** (Figure S9), implying that the framework integrity of **1** was retained. Thus, the turn-off sensing mechanism could not be due to the collapse of the framework. Ultimately, the mechanism of the quenching effect could be interpreted by UV–vis absorption spectroscopy. The UV–vis absorption band of Cr(VI) oxyanions and the fluorescence emission band of **1** show a small degree of overlap, suggesting that fluorescence quenching was not caused by energy transfer mechanism (Figure S10). However, the large extent of overlap between the UV–vis absorption spectra of $\text{Cr}_2\text{O}_7^{2-}/\text{CrO}_4^{2-}$ and the fluorescence excitation spectrum of **1** demonstrates that the competition of absorption of irradiated light source energy between the $\text{Cr}_2\text{O}_7^{2-}$ and CrO_4^{2-} ions and **1** leads to the high fluorescence quenching efficiencies.

The XRPD patterns of **1** after being treated with Cr^{3+} , Fe^{3+} , and Al^{3+} in water were very similar to that of as-synthesized **1** (Figure S11), suggesting that **1** kept the framework integrity and crystallinity. This excluded the possibility of framework collapse caused fluorescence enhancement. Literature has shown that framework–analyte interactions usually demonstrated one of the most possible mechanisms for fluorescence turn-on detection toward metal ions [12,13,31,40,48,49]. To verify this assumption, IR and X-ray

photoelectron spectroscopy (XPS) spectra were measured. Unfortunately, the IR spectra of **1** did not show significant changes after immersion (Figure S12). Meanwhile, the O 1s and N 1s peaks in the XPS spectra were almost unchanged (Figure S13). These findings indicate that there might be no framework–analyte interactions or that such interactions are too weak to cause spectra change. Thus, the turn-on detection mechanism is not due to the framework–analyte interactions. Interestingly, the UV–vis absorption spectra of **1** after addition of Cr^{3+} , Fe^{3+} , and Al^{3+} exhibited significant increase in the absorbance within the sphere of 300–400 nm (Figure S14), corresponding to the excitation energy used. The results illustrated that the turn-on detection of **1** toward Cr^{3+} , Fe^{3+} , and Al^{3+} can be explained by the absorbance caused enhancement (ACE) mechanism [12,50], meaning that the M^{3+} -treated **1** would release more energy than pristine **1** to demonstrate turn-on effect in the emission process.

4. Conclusions

In summary, a luminescent Cd(II) coordination polymer **1** adopting a 2-D gridlike sq1 layer has been successfully synthesized. Coordination polymer **1** shows strong fluorescence emissions in solvent suspension-phase, making them potential candidates to be employed in sensing $\text{Cr}_2\text{O}_7^{2-}$ and CrO_4^{2-} ions via fluorescence quenching effect and in detecting Cr^{3+} , Fe^{3+} , and Al^{3+} ions via fluorescence enhancement response, with high sensitivity and selectivity. From the fluorescence-sensing mechanism studies, absorption energy competition and absorbance caused enhancement can, respectively, interpret the quenching effect toward Cr(VI) oxyanions and the enhancement effect toward Cr^{3+} , Fe^{3+} , and Al^{3+} metal ions.

Supplementary Materials: The following are available online, Figure S1. Experimental and simulated XRPD patterns for as-synthesized **1**. Table S1. Hydrogen-bonding parameters in **1**. Figure S2. TG curve of **1**. Figure S3. Gas adsorption isotherms for thermally activated **1** conducted at 77 K for N_2 and 195 K for CO_2 . Figure S4. XRPD patterns of **1**: simulated, as-synthesized, and after N_2 and CO_2 adsorption. Figure S5. Fluorescence excitation and emission spectra of NI-mbpy-34, Br-1,3- H_2bdc , and **1** in solid-state, as well as **1** in H_2O suspension-phase at room temperature. Figure S6. Fluorescence intensity traces for the H_2O suspensions of **1** upon incremental addition of $\text{Cr}_2\text{O}_7^{2-}$ and CrO_4^{2-} ions, following the first-order exponential decay. Conditions: $\lambda_{\text{em}} = 414$ nm ($\lambda_{\text{ex}} = 365$ nm). Figure S7. Linear region of fluorescence intensity for the H_2O suspensions of **1** upon incremental addition of $\text{Cr}_2\text{O}_7^{2-}$ and CrO_4^{2-} ions. The following table lists the relevant parameters of LOD for the H_2O suspensions of **1** toward $\text{Cr}_2\text{O}_7^{2-}$ and CrO_4^{2-} ions. Conditions: $\lambda_{\text{em}} = 420$ nm ($\lambda_{\text{ex}} = 365$ nm). Figure S8. Linear region of fluorescence intensity for the H_2O suspensions of **1** upon incremental addition of Cr^{3+} , Fe^{3+} , and Al^{3+} ions. The following table lists the relevant parameters of LOD for the H_2O suspensions of **1** toward Cr^{3+} , Fe^{3+} , and Al^{3+} ions. Conditions: $\lambda_{\text{em}} = 414$ nm ($\lambda_{\text{ex}} = 365$ nm). Figure S9. XRPD patterns of **1** before and after immersing in $\text{Cr}_2\text{O}_7^{2-}$ and CrO_4^{2-} aqueous solutions for 24 h. Figure S10. Spectral overlap between the normalized absorption spectra of $\text{Cr}_2\text{O}_7^{2-}$ and CrO_4^{2-} in aqueous solutions and the normalized excitation and emission spectra of **1** in H_2O suspensions. Figure S11. XRPD patterns of **1** before and after immersing in Cr^{3+} , Fe^{3+} , and Al^{3+} aqueous solutions for 24 h. Figure S12. IR spectra of **1** before and after immersing in Cr^{3+} , Fe^{3+} , and Al^{3+} aqueous solutions for 24 h. Figure S13. XPS high resolution spectra of O 1s and N 1s of **1** before and after immersing in Cr^{3+} , Fe^{3+} , and Al^{3+} aqueous solutions for 24 h. Figure S14. UV-vis spectra of **1** before and after addition of Cr^{3+} , Fe^{3+} , and Al^{3+} .

Author Contributions: J.-Y.W. conceived and designed the experiments; K.-S.L., M.-J.T. and L.-J.H. performed the experiments; M.-J.T., C.-M.W. and J.-Y.W. analyzed the data; C.-M.W. and J.-Y.W. contributed reagents/materials/analysis tools; C.-M.W. and J.-Y.W. wrote the paper. All authors have read and agreed to the published version of the manuscript.

Funding: This research was funded by the Ministry of Science and Technology of Taiwan, grant number MOST 106-2113-M-260-007-, MOST 107-2113-M-260-001-, MOST 108-2113-M-260-002-, and MOST 110-2113-M-019-007-, the National Chi Nan University, the National (Taiwan) Ocean University, and the Ministry of Culture's Bureau of Cultural Heritage, and the APC was funded by the Ministry of Science and Technology of Taiwan, grant number MOST 106-2113-M-260-007.

Institutional Review Board Statement: Not applicable.

Informed Consent Statement: Not applicable.

Data Availability Statement: Not available.

Acknowledgments: We gratefully acknowledge the National Chi Nan University, National (Taiwan) Ocean University, the Ministry of Culture's Bureau of Cultural Heritage, and the Ministry of Science and Technology of Taiwan for the support. We also thank the MOST for providing valuable assistance on research support.

Conflicts of Interest: The authors declare no conflict of interest.

Sample Availability: Samples of the compounds NI-mbpy-34 and 1 are available from the authors.

References

1. Xu, G.-R.; An, Z.-H.; Xu, K.; Liu, Q.; Das, R.; Zhao, H.-L. Metal organic framework (MOF)-based micro/nanoscaled materials for heavy metal ions removal: The cutting-edge study on designs, synthesis, and applications. *Coord. Chem. Rev.* **2020**, *427*, 213554. [[CrossRef](#)]
2. Tchounwou, P.B.; Yedjou, C.G.; Patlolla, A.K.; Sutton, D.J. Heavy Metal Toxicity and the Environment. *Mol. Clin. Environ. Toxicol.* **2012**, *101*, 133–164. [[CrossRef](#)]
3. Coetzee, J.J.; Bansal, N.; Chirwa, E.M.N. Chromium in Environment, Its Toxic Effect from Chromite-Mining and Ferrochrome Industries, and Its Possible Bioremediation. *Expo. Health* **2018**, *12*, 51–62. [[CrossRef](#)]
4. Dayan, A.D.; Paine, A.J. Mechanisms of chromium toxicity, carcinogenicity and allergenicity: Review of the literature from 1985 to 2000. *Hum. Exp. Toxicol.* **2001**, *20*, 439–451. [[CrossRef](#)]
5. Costa, M. Toxicity and Carcinogenicity of Cr(VI) in Animal Models and Humans. *Crit. Rev. Toxicol.* **1997**, *27*, 431–442. [[CrossRef](#)] [[PubMed](#)]
6. Dong, C.; Wu, G.; Wang, Z.; Ren, W.; Zhang, Y.; Shen, Z.; Li, T.; Wu, A. Selective colorimetric detection of Cr(III) and Cr(VI) using gallic acid capped gold nanoparticles. *Dalton Trans.* **2015**, *45*, 8347–8354. [[CrossRef](#)] [[PubMed](#)]
7. Lv, R.; Wang, J.; Zhang, Y.; Li, H.; Yang, L.; Liao, S.; Gu, W.; Liu, X. An amino-decorated dual-functional metal-organic framework for highly selective sensing of Cr(III) and Cr(VI) ions and detection of nitroaromatic explosives. *J. Mater. Chem. A* **2016**, *4*, 15494–15500. [[CrossRef](#)]
8. WHO. *Chromium in Drinking-Water. Background Document for Preparation of WHO Guidelines for Drinking-Water Quality*; WHO/SDE/WSH/03.04/4; WHO: Geneva, Switzerland, 2003.
9. Chen, D.-M.; Zhang, N.-N.; Liu, C.-S.; Du, M. Template-directed synthesis of a luminescent Tb-MOF material for highly selective Fe³⁺ and Al³⁺ ion detection and VOC vapor sensing. *J. Mater. Chem. C* **2017**, *5*, 2311–2317. [[CrossRef](#)]
10. Aisen, P.; Wessling-Resnick, M.; Leibold, E.A. Iron metabolism. *Curr. Opin. Chem. Biol.* **1999**, *3*, 200–206. [[CrossRef](#)]
11. Patidar, R.; Rebarry, B.; Bhadu, G.R.; Paul, P. Fluorescent carbon nanoparticles as label-free recognizer of Hg²⁺ and Fe³⁺ through effective fluorescence quenching in aqueous media. *J. Lumin.* **2016**, *173*, 243–249. [[CrossRef](#)]
12. Tian, X.-M.; Yao, S.-L.; Qiu, C.-Q.; Zheng, T.-F.; Chen, Y.-Q.; Huang, H.; Chen, J.-L.; Liu, S.-J.; Wen, H.-R. Turn-On Luminescent Sensor toward Fe³⁺, Cr³⁺, and Al³⁺ Based on a Co(II) Metal-Organic Framework with Open Functional Sites. *Inorg. Chem.* **2020**, *59*, 2803–2810. [[CrossRef](#)]
13. Zhang, J.; Ren, S.; Xia, H.; Jia, W.; Zhang, C. AIE-ligand-based luminescent Cd(II)-organic framework as the first “turn-on” Fe³⁺ sensor in aqueous medium. *J. Mater. Chem. C* **2020**, *8*, 1427–1432. [[CrossRef](#)]
14. Fan, C.; Huang, X.; Han, L.; Lu, Z.; Wang, Z.; Yi, Y. Novel colorimetric and fluorescent off-on enantiomers with high selectivity for Fe³⁺ imaging in living cells. *Sens. Actuators B Chem.* **2016**, *224*, 592–599. [[CrossRef](#)]
15. Dang, S.; Ma, E.; Sun, Z.-M.; Zhang, H. A layer-structured Eu-MOF as a highly selective fluorescent probe for Fe³⁺ detection through a cation-exchange approach. *J. Mater. Chem.* **2012**, *22*, 16920–16926. [[CrossRef](#)]
16. Nayak, P. Aluminum: Impacts and Disease. *Environ. Res.* **2002**, *89*, 101–115. [[CrossRef](#)] [[PubMed](#)]
17. World Health Organization. *Guidelines for Drinking Water Quality*; World Health Organization: Geneva, Switzerland, 2004; Volume 301.
18. Tian, X.; Murfin, L.C.; Wu, L.; Lewis, S.E.; James, T.D. Fluorescent small organic probes for biosensing. *Chem. Sci.* **2021**, *12*, 3406–3426. [[CrossRef](#)]
19. Zhang, F.; Wang, M.; Zeng, D.; Zhang, H.; Li, Y.; Su, X. A molybdenum disulfide quantum dots-based ratiometric fluorescence strategy for sensitive detection of epinephrine and ascorbic acid. *Anal. Chim. Acta* **2019**, *1089*, 123–130. [[CrossRef](#)]
20. Jin, M.; Mou, Z.-L.; Zhang, R.-L.; Liang, S.-S.; Zhang, Z.-Q. An efficient ratiometric fluorescence sensor based on metal-organic frameworks and quantum dots for highly selective detection of 6-mercaptopurine. *Biosens. Bioelectron.* **2017**, *91*, 162–168. [[CrossRef](#)]
21. Han, Z.; Nan, D.; Yang, H.; Sun, Q.; Pan, S.; Liu, H.; Hu, X. Carbon quantum dots based ratiometric fluorescence probe for sensitive and selective detection of Cu²⁺ and glutathione. *Sens. Actuators B Chem.* **2019**, *298*. [[CrossRef](#)]

22. Sun, X.; Lei, Y. Fluorescent carbon dots and their sensing applications. *TrAC Trends Anal. Chem.* **2017**, *89*, 163–180. [[CrossRef](#)]
23. Hao, Y.; Chen, S.; Zhou, Y.; Zhang, Y.; Xu, M. Recent Progress in Metal–Organic Framework (MOF) Based Luminescent Chemodosimeters. *Nanomaterials* **2019**, *9*, 974. [[CrossRef](#)]
24. Zhang, Y.; Yuan, S.; Day, G.; Wang, X.; Yang, X.; Zhou, H.-C. Luminescent sensors based on metal-organic frameworks. *Coord. Chem. Rev.* **2018**, *354*, 28–45. [[CrossRef](#)]
25. Zhang, J.; Tan, Y.; Song, W.-J. Zeolitic imidazolate frameworks for use in electrochemical and optical chemical sensing and biosensing: A review. *Microchim. Acta* **2020**, *187*, 1–23. [[CrossRef](#)] [[PubMed](#)]
26. Yao, C.-X.; Zhao, N.; Liu, J.-C.; Chen, L.-J.; Liu, J.-M.; Fang, G.-Z.; Wang, S. Recent Progress on Luminescent Metal–Organic Framework-Involved Hybrid Materials for Rapid Determination of Contaminants in Environment and Food. *Polymers* **2020**, *12*, 691. [[CrossRef](#)] [[PubMed](#)]
27. Karmakar, A.; Samanta, P.; Dutta, S.; Ghosh, S.K. Fluorescent “Turn-on” Sensing Based on Metal–Organic Frameworks (MOFs). *Chem. Asian J.* **2019**, *14*, 4506–4519. [[CrossRef](#)]
28. Li, H.-Y.; Zhao, S.-N.; Zang, S.-Q.; Li, J. Functional metal–organic frameworks as effective sensors of gases and volatile compounds. *Chem. Soc. Rev.* **2020**, *49*, 6364–6401. [[CrossRef](#)]
29. Lustig, W.P.; Mukherjee, S.; Rudd, N.D.; Desai, A.V.; Li, J.; Ghosh, S.K. Metal–organic frameworks: Functional luminescent and photonic materials for sensing applications. *Chem. Soc. Rev.* **2017**, *46*, 3242–3285. [[CrossRef](#)] [[PubMed](#)]
30. Su, C.-H.; Tsai, M.-J.; Wang, W.-K.; Li, Y.-Y.; Wu, J.-Y. Engineering Tailored Bifunctional Luminescent Pillared-Layer Frameworks for Adsorption of CO₂ and Sensitive Detection of Nitrobenzene in Water Media. *Chem. Eur. J.* **2021**, *27*, 6529–6537. [[CrossRef](#)]
31. Chuang, P.-M.; Wu, J.-Y. A highly stable Zn coordination polymer exhibiting pH-dependent fluorescence and as a visually ratiometric and on–off fluorescence sensor. *CrystEngComm* **2021**, *23*, 5226–5240. [[CrossRef](#)]
32. Chuang, P.-M.; Huang, Y.-W.; Liu, Y.-L.; Wu, J.-Y. Influence of linker substitution on fluorescence responsive sensing of isostructural coordination polymers: Visual turn-on, ratiometric, and turn-off sensing in water. *CrystEngComm* **2021**, *23*, 2222–2234. [[CrossRef](#)]
33. Huang, Y.-W.; Chuang, P.-M.; Wu, J.-Y. Solvent-Induced Controllable Supramolecular Isomerism: Phase Transformation, CO₂ Adsorption, and Fluorescence Sensing toward CrO₄²⁻, Cr₂O₇²⁻, MnO₄⁻, and Fe³⁺. *Inorg. Chem.* **2020**, *59*, 9095–9107. [[CrossRef](#)]
34. Zhang, J.-R.; Lee, J.-J.; Su, C.-H.; Tsai, M.-J.; Li, C.-Y.; Wu, J.-Y. From lamellar net to bilayered-lamella and to porous pillared-bilayer: Reversible crystal-to-crystal transformation, CO₂ adsorption, and fluorescence detection of Fe³⁺, Al³⁺, Cr³⁺, MnO₄⁻, and Cr₂O₇²⁻ in water. *Dalton Trans.* **2020**, *49*, 14201–14215. [[CrossRef](#)]
35. Jiang, Q.-J.; Lin, J.-Y.; Hu, Z.-J.; Hsiao, V.K.S.; Chung, M.-Y.; Wu, J.-Y. Luminescent Zinc(II) Coordination Polymers of Bis(pyridin-4-yl)benzothiadiazole and Aromatic Polycarboxylates for Highly Selective Detection of Fe(III) and High-Valent Oxyanions. *Cryst. Growth Des.* **2021**, *21*, 2056–2067. [[CrossRef](#)]
36. Wang, C.-M.; Lin, Y.-J.; Pan, M.-F.; Su, C.-K.; Lin, T.-Y. A Highly Stable Framework of Crystalline Zinc Phosphite with Selective Removal, Recovery, and Turn-On Sensing Abilities for Mercury Cations in Aqueous Solutions. *Chem. Eur. J.* **2018**, *24*, 9729–9734. [[CrossRef](#)]
37. Hsieh, J.; Chen, J.-Y.; Li, H.-Y.; Liu, H.-K.; Tu, H.-L.; Wang, C.-M. A Thio-Functionated Zinc Phosphite Exhibiting the Large-Channel Framework and Enhanced Removal Ability of Mercury Ion from Aqueous Solutions. *Dalton Trans.* **2020**, *49*, 11085–11089. [[CrossRef](#)]
38. Li, Y.; Xie, J.-F.; Chang, C.-C.; Wang, C.-M.; Tu, H.-L. Highly Sensitive Detection of Mercury Ions Using Zincophosphite Framework Nanoparticle–Polyaniline Composites. *ACS Appl. Nano Mater.* **2020**, *3*, 9724–9730. [[CrossRef](#)]
39. Wang, C.; Li, J.-R.; Li, Y.; Tu, H.-L.; Tzou, D.-L.; Wang, C.-M. Stable Crystalline Organic–Inorganic Hybrid Indium Phosphate with Dye Removal and Ractopamine Detection Applications. *Inorg. Chem.* **2021**, *60*, 11655–11660. [[CrossRef](#)] [[PubMed](#)]
40. Tsai, M.-J.; Liao, K.-S.; Hsu, L.-J.; Wu, J.-Y. A luminescent Cd(II) coordination polymer as a fluorescence-responsive sensor for enhancement sensing of Al³⁺ and Cr³⁺ ions and quenching detection of chromium(VI) oxyanions. *J. Solid State Chem.* **2021**, *304*, 122564. [[CrossRef](#)]
41. Tzeng, B.; Chang, T.; Wei, S.; Sheu, H. Reversible Phase Transformation and Mechanochromic Luminescence of Zn II -Dipyridylamide-Based Coordination Frameworks. *Chem. A Eur. J.* **2012**, *18*, 5105–5112. [[CrossRef](#)] [[PubMed](#)]
42. Sheldrick, G.M. A short history of SHELX. *Acta Crystallogr. Sect. A Found. Crystallogr.* **2008**, *64*, 112–122. [[CrossRef](#)] [[PubMed](#)]
43. Sheldrick, G.M. Crystal structure refinement with SHELXL. *Acta Crystallogr. Sect. C Struct. Chem.* **2015**, *71*, 3–8. [[CrossRef](#)]
44. Farrugia, L.J. WinGX and ORTEP for Windows: An update. *J. Appl. Crystallogr.* **2012**, *45*, 849–854. [[CrossRef](#)]
45. Spek, A.L. Structure validation in chemical crystallography. *Acta Crystallogr. Sect. D Biol. Crystallogr.* **2009**, *65*, 148–155. [[CrossRef](#)] [[PubMed](#)]
46. Yan, Y.-T.; Zhang, W.-Y.; Zhang, F.; Cao, F.; Yang, R.-F.; Wang, Y.-Y.; Hou, L. Four new metal–organic frameworks based on diverse secondary building units: Sensing and magnetic properties. *Dalton Trans.* **2017**, *47*, 1682–1692. [[CrossRef](#)] [[PubMed](#)]
47. Sun, X.; Yao, S.; Yu, C.; Li, G.; Liu, C.; Huo, Q.; Liu, Y. An ultrastable Zr-MOF for fast capture and highly luminescence detection of Cr₂O₇²⁻ simultaneously in an aqueous phase. *J. Mater. Chem. A* **2018**, *6*, 6363–6369. [[CrossRef](#)]
48. Wang, R.M.; Liu, X.B.; Huang, A.; Xiao, Z.Y.; Zhang, L.L.; Dai, F.N.; Sun, D.F. Unprecedented Solvent-Dependent Sensitivities in Highly Efficient Detection of Metal Ions and Nitroaromatic Compounds by a Fluorescent Barium Metal–Organic Framework. *Inorg. Chem.* **2016**, *55*, 1782–1787. [[CrossRef](#)]

-
49. Yu, M.H.; Hu, T.L.; Bu, X.H. A metal–organic framework as a “turn on” fluorescent sensor for aluminum ions. *Inorg. Chem. Front.* **2017**, *4*, 256–260. [[CrossRef](#)]
 50. Wang, M.; Guo, L.; Cao, D. Metal-organic framework as luminescence turn-on sensor for selective detection of metal ions: Absorbance caused enhancement mechanism. *Sens. Actuators B Chem.* **2017**, *256*, 839–845. [[CrossRef](#)]